

Wide-Angle Imaging Lidar Deployment at the ARM Southern Great Plains Site: Intercomparison of Cloud Property Retrievals

IGOR N. POLONSKY, STEVEN P. LOVE, AND ANTHONY B. DAVIS

Space and Remote Sensing Sciences Group (ISR-2), Los Alamos National Laboratory, Los Alamos, New Mexico

(Manuscript received 1 June 2004, in final form 7 November 2004)

ABSTRACT

The Wide-Angle Imaging Lidar (WAIL), a new instrument that measures cloud optical and geometrical properties by means of off-beam lidar returns, was deployed as part of a multi-instrument campaign to probe a cloud field at the Atmospheric Radiation Measurement (ARM) Southern Great Plain (SGP) site on 25 March 2002. WAIL is designed to determine physical and geometrical characteristics using the off-beam component of the lidar return that can be adequately modeled within the diffusion approximation. Using WAIL data, the extinction coefficient and geometrical thickness of a dense cloud layer is estimated, from which optical thickness is inferred. Results from the new methodology agree well with counterparts obtained from other instruments located permanently at the SGP ARM site and from the WAIL-like airborne instrument that flew over the site during our observation period.

1. Background and outline

The term “lidar”—or light detection and ranging from which the acronym is derived—has traditionally implied a ranging device, with the basic idea being to send out a pulse of light and then to detect returns from objects of interest. The assumption of a one-to-one correspondence between the object location and the instant at which the pulse has returned enables the probing of the inner structure of the medium. Many artificial and natural objects are now investigated using lidar techniques. Even limiting ourselves to monostatic backscattering lidar, we can list seawater, aerosol, optically thin clouds (such as cirrus), natural and artificial fogs, pollution, and smoke.

Conversion of photon travel time to range mandates that contributions from multiple scattering be neglected or somehow discriminated. Largely for this reason, backscatter lidar receivers are generally designed with as narrow a field of view (FOV) as possible in order to restrict the backscattered light to small angles around the transmitted beam's direction. This portion of multiple scattering arising from small-angle scattering has

been successfully modeled (Zege et al. 1994; Bissonnette 1996) and used to obtain extra information about the probed object (Bissonnette et al. 2002). But, for optically thick objects such as dense clouds, the on-beam or even small-angle signal quickly becomes contaminated by a multiple-scattering component that cannot be associated with a particular location inside the cloud. In this case, all ranging information beyond detection of the cloud boundary (ceilometry) is irretrievably lost.

This fundamental difficulty can be overcome by a radically different technique called “off-beam lidar,” first suggested by Davis et al. (1997a,b). Here, instead of restricting the receiver's FOV to reject multiply scattered light, it is made as wide as possible in order to collect essentially all of the multiply scattered returning light. An even more radical departure from the basic idea of lidar remote sensing was recently proposed by Evans et al. (2003), where both the transmitter and the receiver are in fact *inside* the sounded cloud; they call this concept for an airborne platform “in situ” cloud lidar, where there is nothing left of the ranging, only multiple-scattering counts. To make use of the information contained in these off-beam signals, we need a completely new lidar equation.

The principle of off-beam lidar is predicated on the fact that multiple scattering thoroughly samples the interior of the medium. So the characteristics of the re-

Corresponding author address: Igor N. Polonsky, Space and Remote Sensing Sciences Group (ISR-2), Los Alamos National Laboratory, MS-436, Los Alamos, NM 87545.
E-mail: polonsky@lanl.gov

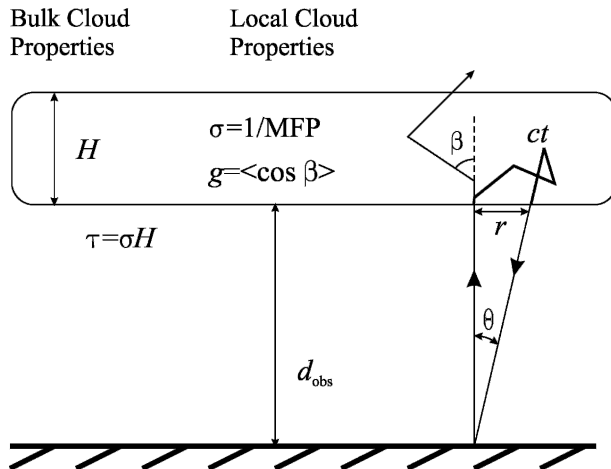


FIG. 1. Geometry of ground-based off-beam lidar observation. See Table 1 for definitions and ranges for the variables and parameters of the problem.

flected radiance distribution in space, angle, and time will depend on its optical and geometrical properties. Photons should be collected within a receiver FOV that is wide enough to take in essentially the entire spatial distribution of the reflected radiance at the medium boundary, and this should enable the retrieval of both geometrical thickness H and a volume-averaged extinction coefficient σ (equivalently, the mean optical depth $\tau = \sigma H$). Figure 1 illustrates schematically cloud observation with a ground-based off-beam lidar, while Table 1 describes the key variables and parameters.

Using scaling arguments from the random walk (i.e., phenomenological diffusion) theory, Davis et al. (1997b) showed that the mean value of t , the time spent by the laser photons inside the cloud before escaping in reflection, is given by

$$\langle t \rangle \propto H/c, \quad (1)$$

where c is the velocity of light, while the root-mean-square (rms) lateral transport distance r between the laser beam and the escape position is given by

$$\sqrt{\langle r^2 \rangle} \propto H/\sqrt{(1-g)\tau}, \quad (2)$$

where g is the asymmetry factor (≈ 0.85 for the dense liquid clouds of interest here). Equation (2) shows that the size of the remotely observable light field excited by the laser, at all times considered, is a relatively weak function of optical depth. It is essentially commensurate with cloud thickness. This immediately sets the following lower bounds on the fields of regard for off-beam lidar devices: $\approx 60^\circ$ for a ground-based system looking at a cloud that is ≈ 1 km thick and ≈ 1 km high,

TABLE 1. Key variables and cloud parameters, with plausible ranges, in ground-based off-beam lidar.

Notation	Definition	Typical range	Units
d_{obs}	Lidar–cloud range ^a	0.5– ∞	km
θ	Observation zenith angle ^b	0–30	$^\circ$
r	$d_{\text{obs}} \tan \theta$, radial distance from beam	≥ 0	km
ct	Photon pathlength inside the cloud	≥ 0	km
H	Cloud geometrical thickness ^c	0.3–3	km
σ	Extinction coefficient	20–200	km^{-1}
MFP	$1/\sigma$, photon mean free path	5–50	m
τ	$\sigma H = H/\text{MFP}$, optical thickness ^d	≥ 6	
β	Scattering angle	0–180	$^\circ$
g	$\langle \cos \beta \rangle$, asymmetry factor	≈ 0.85	

^a The “infinite” range case corresponds to space-based observation where r can be $\gg 1$ km while θ is still within a few mrad. For a successful application of “off beam” lidar techniques to LITE observations of a dense marine stratocumulus layer, see Davis et al. (2001).

^b Our present optics have $\theta_{\text{max}} \approx 27^\circ$, but by moving the beam impact point from the center to the corner of the focal plane image, one can more than double θ_{max} ; as described in the text, this is achieved by mechanically tilting the receiver mount while leaving the transmitted beam vertical.

^c The ability of off-beam lidar to detect more than one cloud layer has yet to be determined. So what we have in mind here is the maximum thickness of a single-layer cloud of the stratus type.

^d The minimum value assigned to τ for off-beam lidar corresponds to $(1-g)\tau \gg 1$ (with $g \approx 0.85$), which is where diffusion theory becomes accurate. This also corresponds roughly to where the on-beam lidar fails to achieve two-way transmission.

and no less than $\approx 6^\circ$ for an airborne system looking at the same low-level cloud from about a 10-km altitude.

Bypassing the derivation by Davis et al. (1997b), one can see that (1) is equivalent to the often repeated but seldom proven statement that the (typical) number of scatterings for reflected light goes as optical depth. Indeed, multiplying both sides of (1) by σc we see that $\langle \sigma ct \rangle$, the mean *optical* path inside the cloud (which is incremented by unity at each scattering), is proportional to $\sigma H = \tau$. Physically speaking, there is an expanding “cloud” of photons spreading into the cloudy medium at a rate that would be given by the classic law of diffusion (Einstein 1905),

$$\langle r^2 \rangle = Dt, \quad (3)$$

were it not for cloud boundary effects. Here $D = c l_t/3$ denotes photon diffusivity that depends only on the “transport” mean free path $l_t = 1/(1-g)\sigma$. Using (1) to determine t in (3), as a rough estimate of when photons return to the illuminated boundary, yields $\langle r^2 \rangle \approx l_t H$, which is equivalent to (2). Davis et al. (1999) used rig-

orous diffusion theory in finite media to improve the basic off-beam lidar relations in (1)–(2), thus, providing exact $O(1)$ proportionality constants and correction terms that are dependent on $(1 - g)\tau$. These corrections are not insignificant in the observed range of τ . In all of this, photon absorption is assumed to be inconsequential, which is why the diffuse radiance field excited by the pulsed laser on one boundary can permeate the whole cloud, and, thus, be exploited as suggested in (1) and (2) to extract H and τ .

Off-beam lidar can therefore compete with millimeter-wavelength cloud radar (MMCR) as a probe of cloud structure in the sense of height, thickness, and density. It will, of course, not yield the same spatial detail as millimeter-wavelength radar because lidar-based estimates of H and τ are inherently averaged over a horizontal scale that is commensurate with (2), and detailed stratification information is not available. (We discuss ways of inferring internal cloud variability from off-beam signal analysis in our closing remarks, and the ability of off-beam lidar to detect more than one cloud layer has yet to be determined.) In millimeter-wavelength radar, reflectivity is, however, weighted toward the largest droplets. It responds, therefore, very strongly to drizzle, so much so, in fact, that radiative and microphysical quantities of interest in climate studies, including the lower cloud boundary, are all but lost (Clothiaux et al. 1995). We view off-beam lidar as a natural extension of on-beam lidar and as a complement to millimeter-wavelength radar at a visible wavelength that bears directly on the climatic impact of clouds.

It is interesting to recall here the venerable history of using steady-state diffusion theory in cloud remote sensing. Indeed, Meador and Weaver (1980) showed that all two-stream approximations in atmospheric radiative transfer theory are mathematical variants of the 1D diffusion equation that was first solved in this context by Schuster (1905). As an example germane to the ground-based remote sensing of clouds, the methodology advanced by Min and Harrison (1996) is ultimately based on diffusion theory, as is most cloud remote sensing in the solar spectrum. Operational implementation of techniques based on multistream solutions of the 1D radiative transfer problem is indeed a relatively recent development (e.g., Nakajima and King 1990). Outside of off-beam and in situ lidars, the last conscious effort to exploit diffusion theory in a new cloud-probing instrument we know about is by King (1986). His cloud absorption radiometer was designed for airborne in-cloud operation and was successfully deployed by King et al. (1990) in a marine stratocumulus layer. As anticipated, these authors found the characteristic angular

signature of diffusion in dense clouds, which later motivated the phenomenology of radiative smoothing (Cahalan and Snider 1989; Marshak et al. 1995; Davis et al. 1997a). Radiative smoothing theory, which is ultimately based on (2), not only contributed to finding the resolution (satellite pixel size) and other conditions at which the modeling error in cloud remote sensing due to the 1D assumption is at a minimum, but also led to the concept of off-beam lidar (Davis et al. 1997a).

Davis (1999) extended the temporal scaling argument that yields (1) to show that

$$\langle I^2 \rangle \propto (1 - g)\tau(H/c)^2, \quad (4)$$

which is a prediction confirmed and refined by the analytical diffusion theory of Davis et al. (1999). Bringing together (1) and (4) demonstrates that H and τ can, in principle, be derived from temporal observations alone. This was independently verified by Miller and Stephens (1999) using detailed Monte Carlo results for spaceborne lidar geometry, while Davis et al. (2001) successfully applied their two-moment temporal method to data collected over clouds during the Lidar in Space Technology Experiment (LITE). Furthermore, the time domain retrieval method developed by Evans et al. (2003) for in situ cloud lidar confirms that waveforms alone contain enough information to infer cloud properties.

Inspired by the simple relations in (1)–(2) and (4), the first versions of the off-beam cloud lidar technique were based on estimation of the spatial and temporal moments of the radiance distribution. This assumes that these distributions are measured over a wide enough range in t and r , maybe twice the values of the low-order moments in (1)–(2). As shown further on, this is not always possible. The theory was further developed by Polonsky and Davis (2004), allowing one to estimate analytically the corresponding distributions. We shall use these new formulas here to retrieve cloud properties even when the distributions are quite severely truncated in the observations.

The above scaling arguments provided a compelling rationale to create the first prototype of a ground-based off-beam lidar system. This device, called Wide-Angle Imaging Lidar (WAIL), was deployed in field experiments near Los Alamos, New Mexico (Love et al. 2001, 2002). We thus demonstrated that, even with a relatively modest laser (0.5 mJ per pulse), reflected radiance was readily detected with existing technology out to $\approx 30^\circ$ off zenith for a 1-km cloud ceiling. We also showed that the moment-based retrieval algorithms for geometrical and optical thickness outlined above gave reasonable results. But, lacking independent measurements of the cloud properties in those

early experiments, the qualification of “reasonable” was based on visual assessment of the clouds of opportunity.

Here, for the first time, WAIL was deployed alongside other cloud-probing systems: a microwave radiometer (MWR) (Liljegren 1994), a millimeter-wavelength cloud radar (Moran et al. 1998), a ceilometer (Lonnqvist 1995), and a micropulse lidar (MPL; Spinhirne 1993). This suite of Atmospheric Radiation Measurement (ARM) instruments was used to sound an extensive cloud layer above the Oklahoma Southern Great Plains (SGP) site during the night of 24–25 March 2002 thus enabling a direct comparison of WAIL with other instruments. In addition to these ground-based instruments, another off-beam lidar system, Cloud Thickness from Offbeam Lidar Returns (THOR), was looking down at the same cloud system from the National Aeronautics and Space Administration’s (NASA’s) P-3B aircraft; THOR’s design and performance are described by Cahalan et al. (2005). For our present purposes, THOR’s on-beam channel provided yet another estimate of cloud-top altitude although not immediately above head.

In this article we use the recently developed diffusion theory by Polonsky and Davis (2004) to retrieve cloud parameters from WAIL data. The particular cloud field that prevailed during our joint observation period was less than ideal for WAIL in its current configuration; the ceiling was never above 0.5 km, so WAIL’s 53.6° full-width FOV was insufficient to capture the entire spatial radiance pattern emanating from the relatively thick ($H \approx 0.5\text{--}0.7$ km) and opaque ($\tau \approx 15\text{--}30$) cloud. This handicap notwithstanding, the new theory still yields good retrievals from the truncated distributions.

In the following section we describe the WAIL instrument and compare the current version with a previous incarnation discussed in earlier papers. In section 3, the required diffusion theoretical results are surveyed without derivations, but their accuracy is verified by comparison with detailed Monte Carlo simulations. Section 4 gives observational details about the March 2002 deployment at the ARM site in Oklahoma. Analyses of selected WAIL data from that collection are presented in section 5, yielding estimates of cloud parameters. These retrievals are compared with independent estimates in section 6. In section 7, we summarize our findings and outline future work on the instrumental and theoretical aspects of off-beam lidar.

2. The WAIL instrument system

WAIL is a fully imaging implementation of the off-beam lidar concept. The basic idea is to send a narrow-

beam, short-pulse laser into a cloud, an excitation approximating a Dirac δ function in both space and time, and to monitor the returning light at high temporal and spatial resolution. In essence, one collects a high-speed “movie” of the returning light that is, by definition, a physical manifestation of the cloud’s Green’s function for the time-dependent radiative transfer equation. For ground-based measurements, this must be done over a very wide FOV that is sufficient to take in a roughly kilometer-wide expanse of cloud, commensurate with the cloud layer’s physical thickness. With cloud bases typically on the order of 1 km above the ground, the required full-angle FOV is about 1 rad.

In earlier work (Love et al. 2001, 2002), we described a realization of WAIL based on a novel microchannel-plate (MCP)/crossed delay line (CDL) photon-counting imager developed at Los Alamos National Laboratory. This powerful new type of low-light imaging system was described in detail by Priedhorsky et al. (1996). The MCP/CDL detector system’s extremely high time resolution (100 ps) and excellent low-light sensitivity made it attractive for our prototype WAIL experiments, including some early laboratory-scale simulations of off-beam lidar (100 ps corresponds to a path of only 3 cm), where the “cloud” was a moderate-sized aquarium filled with a scattering liquid suspension (Davis et al. 1998).

The MCP/CDL’s main disadvantage for WAIL arises from its unique method of imaging. It relies upon accurately timing the photoelectron pulses, originating from individual photon impacts, that emerge from the two orthogonal delay lines. This timing-based imaging scheme becomes confused when flux over the entire detector exceeds roughly 5×10^6 photons per second thus placing a firm upper limit on the amount of light that can be admitted into the system. This constraint becomes problematical for off-beam lidar experiments on clouds, because of the orders-of-magnitude dynamic range between the bright initial return and the long time and large displacements returns that are of particular interest here.

We therefore developed a second implementation of WAIL, used for the measurements described in this paper, employing a commercial (Roper Scientific, Princeton Instruments “PI-Max”) gated, intensified charge-coupled device (CCD) as the receiver. This detector technology, like the MCP/CDL, uses a microchannel plate photomultiplier, but there the similarity ends. The CCD system has an ultimate time resolution of 2 ns, compared to 100 ps for the MCP/CDL, but this difference is unimportant for cloud measurements where relevant time scales are tens of nanoseconds and longer. More important are the differences in the basic

modes of operation. Unlike the MCP/CDL system, which time tags each photon individually, the gated CCD system achieves time resolution by electronically gating the intensifier, with gate width and gate delay relative to the laser pulse as adjustable parameters. The MCP/CDL system collects an entire time series for each laser pulse (although only a few photons per pulse can be collected), with good statistics achieved by integrating results over many pulses. The gated CCD, in contrast, collects many photons during its narrow time gate, at a specific delay after the laser pulse, again integrating multiple pulses to achieve good statistics; then it advances the gate delay to collect the next movie “frame.”

There are two main advantages of the gated CCD system. First, it can collect many more photons per laser pulse than the MCP/CDL system. Second, the adjustable gate width of the CCD system allows the exposure time to be adjusted automatically during the course of the measurement, with short exposures for the bright early returns, and longer exposures for the dim high-order scattering. This considerably ameliorates the problems caused by the large dynamic range of the cloud-scattered returns.

This time domain strategy for dealing with the large dynamic range of typical cloud WAIL returns is an important improvement over our previous WAIL instrument. However, we continue to use our earlier spatial domain method to suppress the bright central peak that is associated with the initial laser impact on the cloud. This method uses the strong angular dependence of the wavelength passed by bandpass interference filters, which are used in any case to minimize contamination by background light. For a bandpass filter centered at a wavelength somewhat longer than the laser wavelength, the laser will be outside the passband at normal incidence, but the filter’s passband will be shifted to the laser wavelength for a range of off-normal angles. Figure 2 illustrates this effect for our collection of 10-nm bandpass filters. To obtain unsaturated data with good signal-to-noise ratios for the entire angular range, we typically collect data using two or three filters with overlapping angular passbands, then splice the datasets to form a complete dataset covering the full angular range. Subsequent to the measurements described in this paper, we have found that this rather awkward splicing procedure can be avoided entirely by using a single filter with a wider bandpass that admits the full range of angles while still sufficiently reducing background light; the CCD’s temporally variable integration time alone can cope with the wide dynamic range.

We use a high-repetition-rate, low-energy-per-pulse

laser, and average over many pulses to attain good statistics, effectively making our system an imaging version of a micropulse lidar. Though the laser is used without any beam-expanding optics, the laser’s intrinsic 3-mrad full-angle divergence spreads the beam sufficiently to become eye safe at ranges greater than 1 km, significantly reducing the hazards to aircraft. The laser used here is a frequency-doubled neodymium-doped yttrium–aluminum–garnet (Nd:YAG) (Cutting Edge Optronics “Stiletto”), with a 30-ns pulse width, and pulse energy of approximately 0.5 mJ with a 4-kHz repetition rate.

WAIL’s CCD imager uses a 512×512 pixel array, but for the weakly variable cloud decks encountered here, such high spatial resolution is not required. Therefore, to keep data volumes more manageable, we use 4×4 on-chip binning to reduce the spatial sampling to an effective 128×128 pixels. The CCD camera is equipped with a commercial 12.5-mm-focal-length lens, resulting in a square FOV at the focal plane, with 53.6° on a side ($\approx 0.42^\circ \times 0.42^\circ$ per pixel). The lens speed was set at $f/1.3$.

The FOV and angular mapping as a function of field position were directly measured in the laboratory, using targets placed at measured distances from the camera and at measured displacements from the camera’s central axis. We find that the lens’s angular mapping onto the CCD image plane is nearly linear, with the angular width of an individual pixel varying by less than 10% across the image, from 0.397° at the center of the image to 0.435° at the edges.

The spatial variation of the photometric response of the complete CCD–lens–filter system was calibrated in the laboratory for each interference filter, using a 30-cm-diameter integrating sphere with a 10-cm aperture, illuminated with the 532-nm laser to produce a spatially uniform calibration target. The camera lens was placed at the sphere aperture and full-frame images of this uniform target were obtained for each of the interference filters. After subtracting dark counts, the result is a set of two-dimensional relative spatial response functions that are used to correct all subsequent field data. This method takes into account not only the filter’s angular response, but also lens vignetting and intrinsic variations in the CCD.

Figure 3 shows the two versions of WAIL in field deployments. The laser transmitter is the same for both cases; only the imaging system and associated lenses have changed. The movielike nature of the WAIL datasets can be seen in Fig. 4, which shows four representative 2D “stills” from each of three WAIL movies—one for each of the three filters in Fig. 2. These data, obtained using the CCD version of WAIL de-

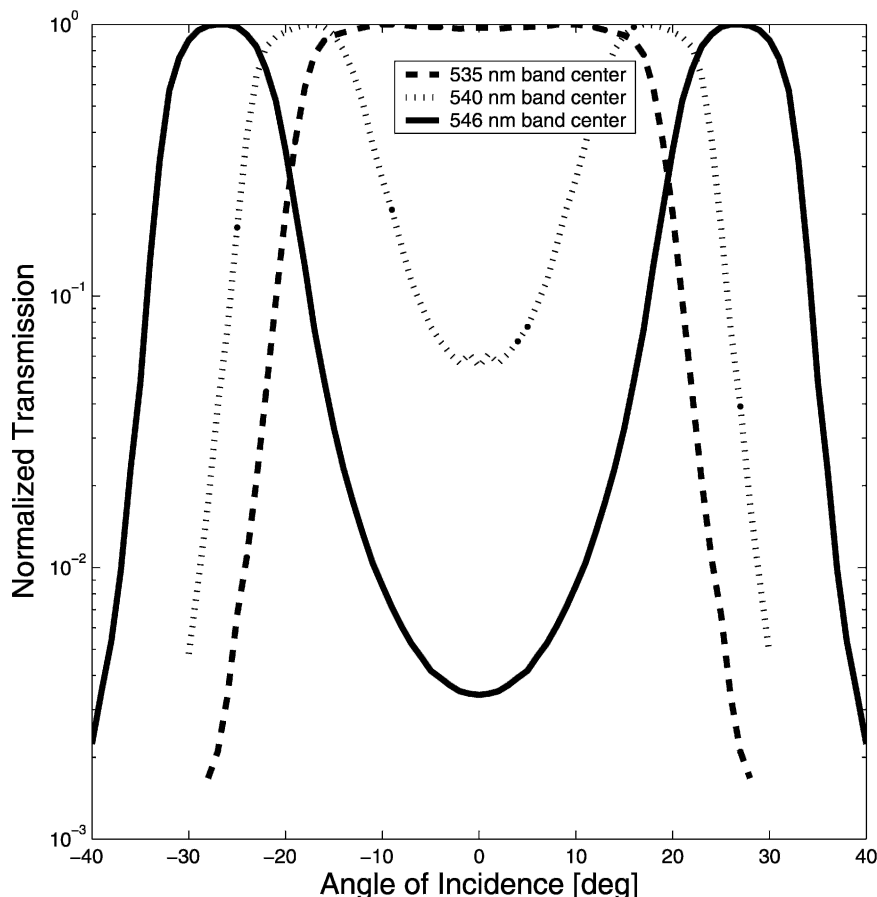


FIG. 2. Bandpass interference filters as angular response filters. Transmission at 532 nm as a function of angle of incidence for our 10-nm bandpass interference filter collection. The band centers listed in the figure refer to normal incidence. The filter's center wavelength shifts to shorter wavelengths for off-normal incidence, leading to an angularly varying transmittance for a given fixed wavelength. This effect is used to suppress the bright central spot of cloud WAIL returns.

ployed in Oklahoma, are part of the dataset analyzed further on. Each of the sequences shown in Fig. 4 begins with the impact of the laser pulse on the cloud bottom, followed by spreading the light via multiple scattering within the cloud. The leftmost sequence, obtained using the center-weighted (535 nm) filter (cf. Fig. 2), most closely approximates the qualitative behavior of the space–time Green's function—spreading and dimming. The sequences on the right (540 and 546 nm) contain information from larger backscattering angles and illustrate two phenomena of interest. First, note how the early time, on-beam signal is strong enough to be visible despite these filters' orders-of-magnitude normal incidence attenuation of the 532-nm laser wavelength (cf. Fig. 2). Second, note how at later times the photons escaping the cloud base at large distances from the beam eventually populate the angular annulus of admittance for these off-beam filters.

3. Off-beam lidar signal modeling with diffusion

To interpret the WAIL data described above and extract physical information about the probed cloud, we need a realistic theory for the off-beam lidar signal. For this, we will invoke photon diffusion theory. In this section, we summarize the diffusion-based forward model the off-beam lidar signal used further on to infer geometrical cloud thickness and volume-averaged extinction and hence mean optical depth.

a. Definitions and assumptions

The schematic in Fig. 1 shows the geometry of ground-based off-beam lidar observation. In the case of a simple conservatively scattering homogeneous “slab” cloud, the basic quantities are geometrical thickness (H) and extinction coefficient (σ). In diffusion theory, the only characteristic of the phase function that mat-

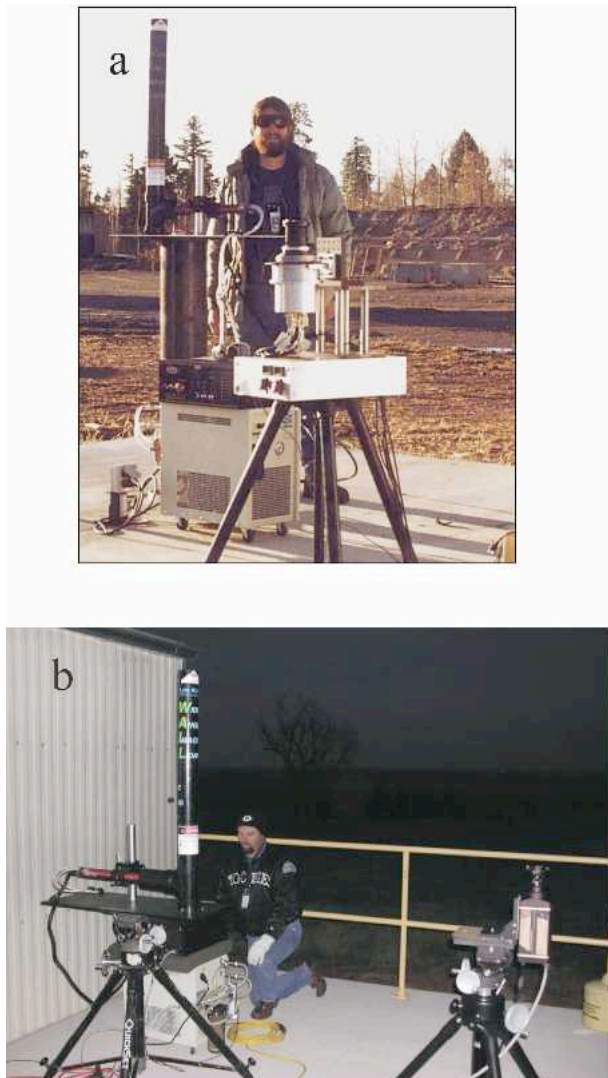


FIG. 3. Two incarnations of the WAIL system for cloud observations: (a) the MCP/CDL version of WAIL, deployed at Fenton Hill Observatory, NM, in Apr 1999 [see Love et al. (2001) for results from this standalone WAIL campaign]; and (b) the gated intensified CCD version, deployed at the ARM SGP site near Lamont, OK, in Mar 2002. The laser transmitter is the same for both versions.

ters is the mean cosine (g) of the scattering angle. To fully characterize our cloud-sounding scheme we also need the distance between the lidar and the illuminated cloud boundary (d_{obs}). Table 1 summarizes these definitions, gives derived quantities, and provides some typical ranges.

The cloud homogeneity assumption used here is of course questionable. Although we are confident it did not cause much damage here, it is high priority to develop diffusion-based models with both vertical and horizontal variability parameters. Our previous exer-

cises in moment-based/time-only retrievals used ground-based (Love et al. 2001) and space-based (Davis et al. 2001) off-beam signals, and these studies established that the primary concern is vertical stratification of extinction in clouds driven by lift, radiation, and microphysical processes. As for the horizontal variability driven by turbulence, Davis et al. (1997a) found an $\approx 10\%$ effect in their early numerical simulations of laser beam propagation in fractal cloud models, a bias that is captured accurately by the analytical approach used by Davis et al. (2002) for transmission statistics. This is for the observables (low-order moments) in (1)–(2); the retrieved cloud properties H and τ are affected at the same level or less. The reason for this is that, being fractal in nature, horizontal fluctuations in optical depth have long-range correlations (several tens of kilometers) and we are only interested in variance over a scale on the order of $\sqrt{\langle r^2 \rangle}$ in (2), a kilometer or so at most (using the mean τ in the formula).

b. Diffusion theoretical model and boundary layer corrections

To describe the WAIL signal, we use the diffusion framework (Ishimaru 1978) and follow Polonsky and Davis (2004) closely, but not exactly. Accordingly, we assume that boundary radiance, $I(t, \mathbf{r}, \mathbf{n})$, in the direction \mathbf{n} [measured in coordinates (θ, ϕ) where θ is measured away the vertical z axis] at position \mathbf{r} (a 2D vector) and time t (after the pulse hits the lower cloud boundary) can be written

$$I(t, \mathbf{r}, \mathbf{n}) = G(t, \mathbf{r})u(\mathbf{n}), \quad (5)$$

where $G(t, \mathbf{r})$ is the reflective boundary Green's function for a collimated source beam (normal to the boundary), and the angular distribution of reflected radiance is factored into $u(\mathbf{n})$. Letting c denote the speed of light, diffusion theory delivers our new lidar equation in a closed form as

$$G(t, \mathbf{r}) = \frac{\pi}{t(H + 2\chi)^2} \exp\left[-\frac{\mathbf{r}^2}{2\chi ct}\right] \sum_{m=1}^{\infty} m \sin\left(\frac{5\pi\chi m/2}{H + 2\chi}\right) \exp\left[-\frac{\chi ct}{2} \left(\frac{\pi m}{H + 2\chi}\right)^2\right], \quad (6)$$

where we adopt the classic (Eddington 1916) expression for the “extrapolation” length

$$\chi = \frac{2/3}{(1 - g)\sigma} \quad (7)$$

(slightly different numerator values have been proposed), and

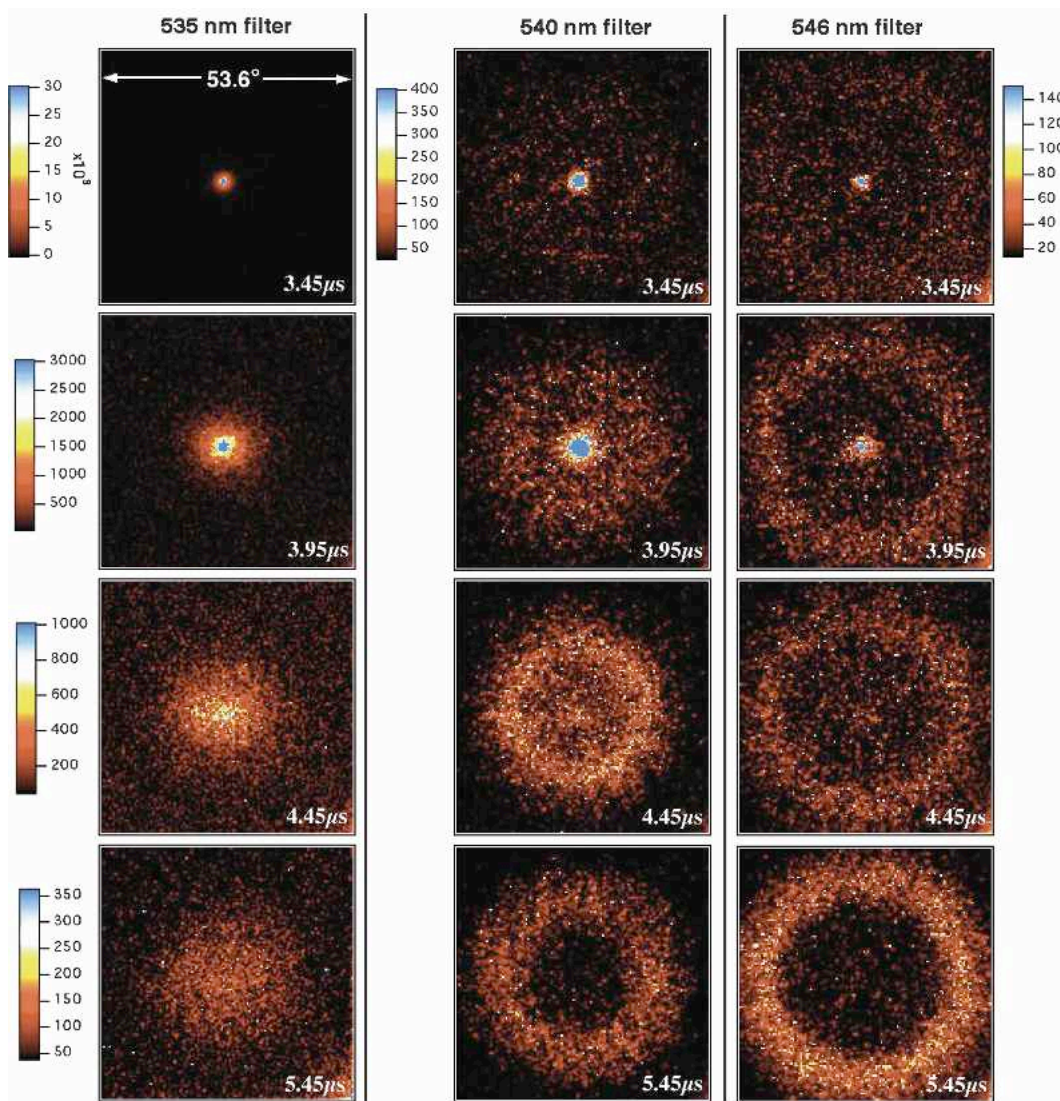


FIG. 4. Sample frames from WAIL datasets obtained at the Oklahoma CART site between 0723 and 0735 UTC 25 Mar 2002. Shown here are sequences obtained using three different background suppression interference filters that optimize for different ranges of observation angle. The first (535-nm nominal band center) emphasizes the central, small-angle region, the second (540 nm) emphasizes the intermediate region, and the third (546 nm) emphasizes large angles (cf. Fig. 2). Each frame has a 53.6° square FOV. The time delay after the laser pulse is noted on each frame. The color scales are adjusted as needed to visualize the image. In each sequence, one sees the initial impact of the laser pulse on the cloud, with subsequent decay and diffusive spreading of the light via multiple scattering. The annular appearance of the scattered distribution, seen at long times in the sequences for the 540- and 546-nm filters, is an artifact of those filters. The illuminated area seen in the bottom row illustrates the approximate useful range of angles for each filter.

$$u(\mathbf{n}) = \frac{1}{4\pi} \left(1 + \frac{3}{2} \cos\theta \right). \quad (8)$$

We recognize here $1/(1 - g)\sigma$ as the “transport” or “rescaled” mean free path of the photons.

Integration of (5) over t yields the steady-state version of the diffusion solution:

$$I(\mathbf{r}, \mathbf{n}) = G(\mathbf{r})u(\mathbf{n}), \quad (9)$$

where (6) leads to

$$G(\mathbf{r}) = \frac{\pi}{(H + 2\chi)^2} \sum_{m=1}^{\infty} m \sin\left(\frac{5\pi\chi m/2}{H + 2\chi}\right) K_0\left(\frac{\pi m r}{H + 2\chi}\right), \quad (10)$$

where K_0 is the zeroth-order modified Bessel function.

The main differences between the above expressions

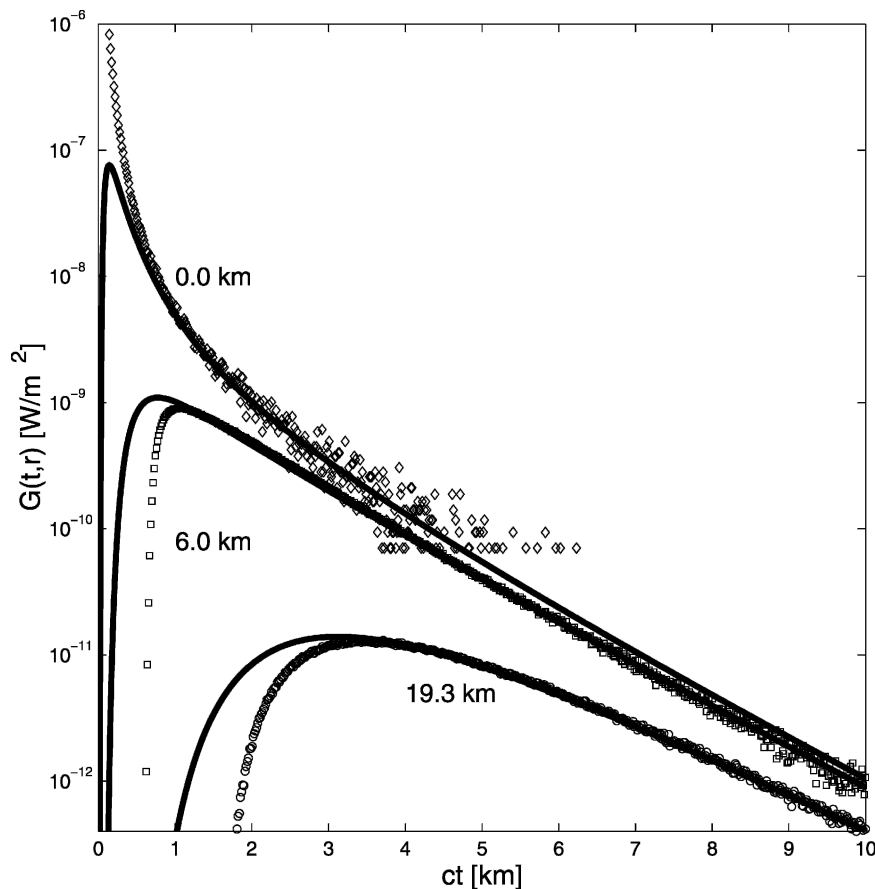


FIG. 5. Boundary flux $G(t, r)$ as a function of ct for a 1-J pulse. Diffusion approximation predictions are shown by solid black lines while Monte Carlo results are depicted by the symbols. The values at the curves are radial distance. Cloud geometrical thickness is 0.7 km and optical thickness is 25. The phase function is highly forward peaked (Deirmendjian Cloud C.1).

for the off-beam lidar signals and the counterparts for the space-time and space-only Green's functions given by Polonsky and Davis (2004) is that 1) they were not concerned with the flux-to-radiance conversion term $u(\mathbf{n})$, and 2) they addressed the problem of embedded isotropic point sources. Rather than integrating the point-source Green's function over the appropriate exponential distribution, we start with a simpler asymptotic theoretical expression for the collimated beam problem. Minor differences arise in the m dependence of the coefficients of the exponential and Bessel function terms in the summations. As was the case for Polonsky and Davis (2004), one needs to invoke the Poisson sum rule to convert the slowly converging series obtained by time integration of (6) into the above-mentioned rapidly converging series in (10). For a full derivation, we refer to Polonsky and Davis (2005).

What is the accuracy of the above diffusion-based expressions? A priori, we trust (6), (7), and (10), but

not (8), because diffusion is known to lose accuracy in the angular domain at the cloud boundaries.

To make this assessment, we performed Monte Carlo simulations for a homogeneous cloud with a (Deirmendjian 1969) Cloud C.1 phase function and a geometrical thickness of 0.7 km at a range of 0.5 km. A forward Monte Carlo scheme using 10^9 trajectories was used. The laser source generates a δ pulse with unit energy so time dependencies of the boundary flux $G(t, \mathbf{r})$ at selected radial distances were obtained by Monte Carlo simulation, and with (6) and (7). Results are plotted in Fig. 5, showing that diffusion accurately describes the time dependence starting at an instant dependent on the radial distance. Similarly, we plot results for $G(\mathbf{r}) \equiv G(r)$ as a function of radial distance for the steady-state case (Fig. 6). For the diffusion approximation in (10), results were multiplied by the factor of 0.83 to emphasize the similarity. The need for this kind of adjustment is traceable (Davis et al. 1999; Polonsky

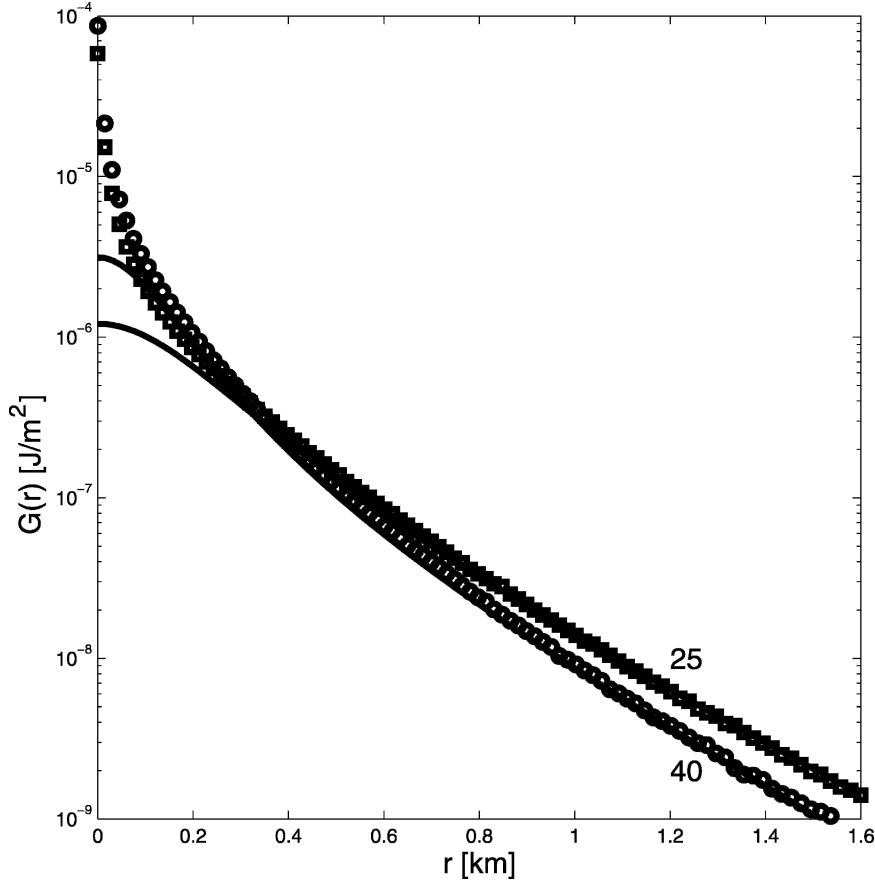


FIG. 6. Boundary flux $G(r)$ as a function of r for a 1-J pulse. Diffusion approximation predictions are shown by solid black lines while Monte Carlo results are depicted by symbols. The values at the curves are cloud optical thickness. Cloud geometrical thickness is 0.7 km and the scattering phase function is Deirmendjian Cloud C.1.

and Davis 2004) to the choice of $2/3$ as numerator in (7) for χ , a boundary condition parameter in diffusion theory. This quantity indeed appears in all of the sin functions used in the expansion (10).

Finally, we need to examine the accuracy of (5) with (8) for the angular dependence of the radiance. Given (5), the azimuthally integrated lidar signal $F(t, \theta)$ is

$$F(t, \theta) = 2\pi \left(\frac{\cos\theta}{d_{\text{obs}}} \right)^2 G(t, r = d_{\text{obs}} \tan\theta) u(\cos\theta), \quad (11)$$

and we will denote its time integral by $F(\theta)$. This provides us with a simple way to check the parameterization by comparing $u(\cos\theta)$ in (8) with the ratio

$$R(t, \theta) = \left(\frac{\cos\theta}{d_{\text{obs}}} \right)^2 \frac{F(t, \theta)/2\pi}{G(t, d_{\text{obs}} \tan\theta)} \quad (12)$$

for selected instants in time, using Monte Carlo to estimate the numerator. Results are displayed (see Fig.

7). As expected, we see that $R(t, \theta)$ is substantially different from $u(\cos\theta)$ only at small ct and approaches the diffusion prediction at a large enough ct , that is, in the asymptotic regime where we make our retrievals. For the steady-state solution, we compute the ratio

$$\begin{aligned} R(\theta) &= \left(\frac{\cos\theta}{d_{\text{obs}}} \right)^2 \frac{\int_0^\infty F(t, \theta) dt / 2\pi}{\int_0^\infty G(t, d_{\text{obs}} \tan\theta) dt} \\ &= \left(\frac{\cos\theta}{d_{\text{obs}}} \right)^2 \frac{F(\theta)/2\pi}{G(d_{\text{obs}} \tan\theta)}. \end{aligned} \quad (13)$$

Results for several cloud optical thicknesses and lidar-cloud distances are plotted (see Fig. 8), showing deviations of $R(\theta)$ from the literal prediction of the diffusion approximation in (8) that need to be corrected. This is basically WAIL's radiance-to-flux conversion and the empirical function

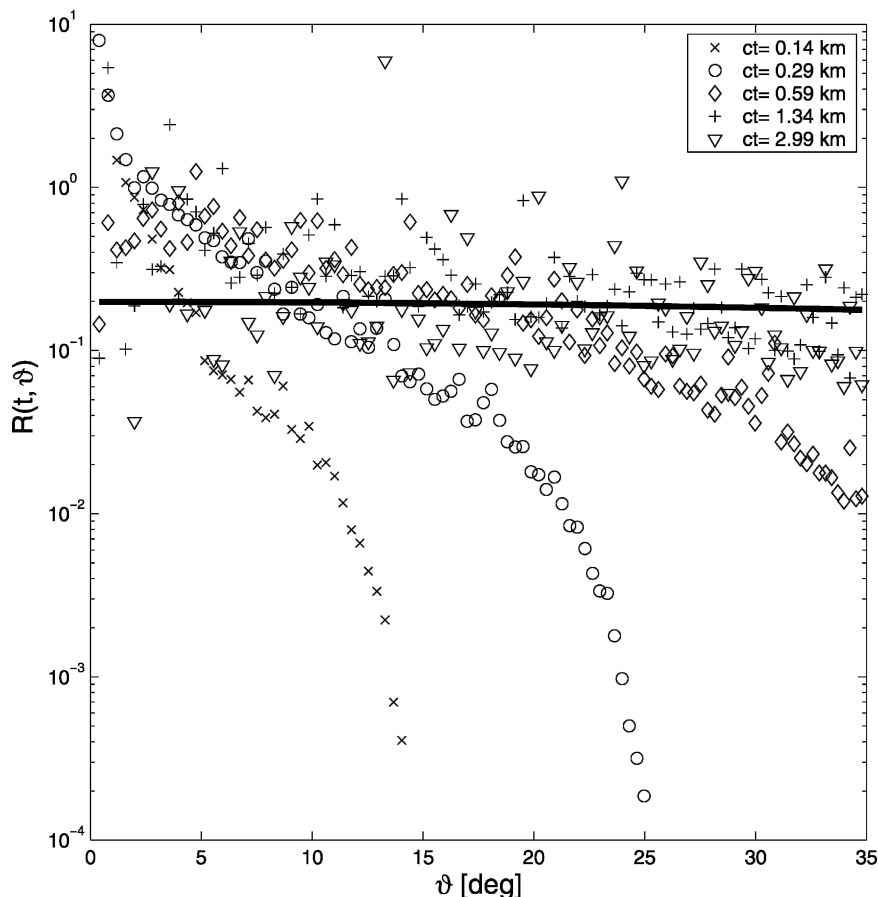


FIG. 7. Ratio $R(t, \theta)$ in Eq. (12) as a function of the observation angle θ for several values of ct . The strict diffusion prediction $u(\cos \theta)$ in Eq. (8) is shown by the solid line. The cloud optical thickness is 20 and its geometrical thickness is 0.7 km; distance to the cloud is 0.5 km. The phase function is Deirmendjian Cloud C.1. The early times ($ct < 1$ km) where (8) fails systematically were not used in our retrievals of dense cloud properties.

$$u_{\text{emp}}(\theta) = \text{const} \times \exp(5.6 \cos \theta), \quad (14)$$

shown by the dashed lines, provides a reasonable approximation independently of cloud parameters (because the multiplicative constant absorbs the overall reflectance value dependent on τ). We will use this empirical relation to estimate flux $G[\theta = \arctan(r/d_{\text{obs}})]$ at the cloud boundary from the observed lidar signal $F(\theta)$ in the steady-state case.

4. The March 2002 ARM site deployment

The data described and analyzed here were obtained at one of the U.S. Department of Energy (DOE) ARM program's Cloud and Radiation Testbed (CART) sites. Specifically, WAIL was deployed at the SGP site in north-central Oklahoma simultaneously with overflights by NASA's THOR instrument. Cahalan et

al. (2005) give a comprehensive overview of the synoptic situation. The data analyzed here were collected between 0730 and 0800 UTC when the cloud base was at its maximum height during the observation period. This gives us the widest possible sampling of the off-beam signal distribution, although it is still quite severely truncated compared to previous deployments (Love et al. 2001, 2002).

As discussed above, both angular and temporal strategies for mitigating the large dynamic range were used. Each complete dataset consists of the following three pieces obtained sequentially: a dataset using an interference filter nominally centered at 535 nm, showing scattering in the central region near the initial laser impact on the cloud; another obtained with a 540-nm filter, emphasizing intermediate viewing angles (roughly between 10° and 20°); and a third obtained using a 546-nm filter for the largest viewing angles.

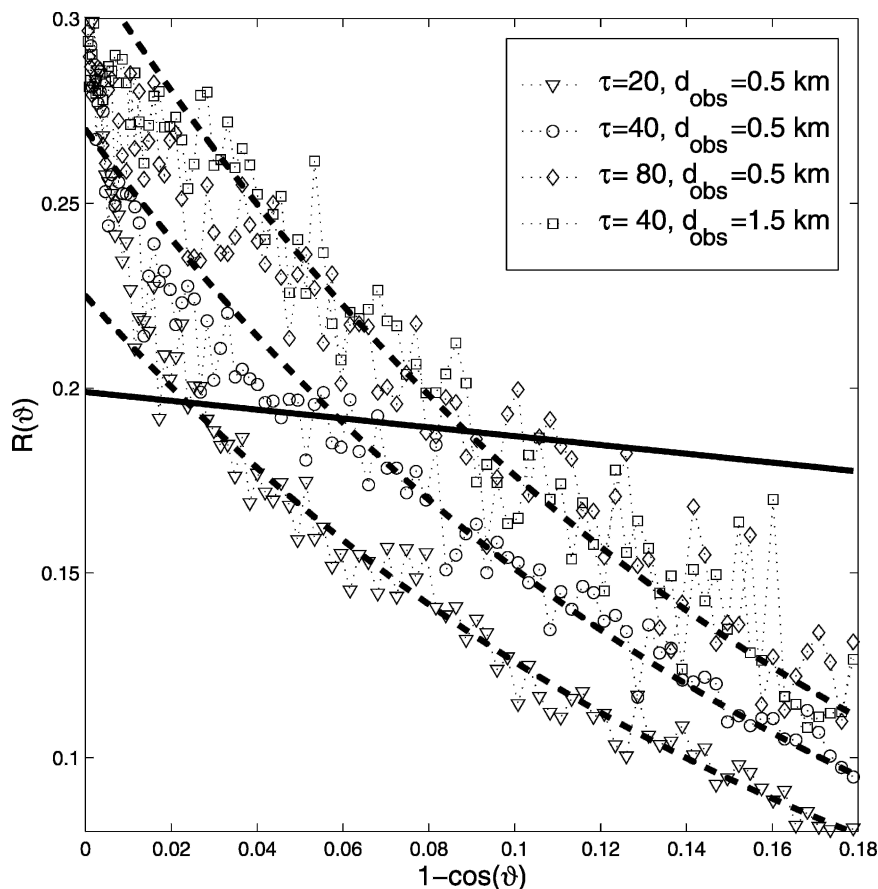


FIG. 8. Ratio $R(\theta)$ in Eq. (13) as a function of $1 - \cos\theta$ for several values of the cloud optical and distance to the cloud. Cloud thickness is held constant at 0.7 km and the phase function is Deirmendjian model Cloud C.1. The strict diffusion prediction $u(\theta)$ in Eq. (8) is shown by the solid line. The dashed lines depict our empirical radiance-to-flux correction factor in Eq. (14).

Each dataset consists of 301 frames, having gate delays ranging from 0.70 to 15.70 μs after the laser pulse, with a constant gate delay increment of 50 ns. For each of these datasets, the CCD gate width was increased linearly with time, ranging from 5 to 100 ns for the small scattering angle data, and from 50 to 250 ns for the two wider-angle datasets. Eventually the integration time becomes longer than the delay increment for the latter part of each dataset. The 50-ns increment refers to the beginning of each integration period. Thus, for later frames, the integration periods for adjacent frames overlap. This has little effect on the end result because the multiple scattering decay is slowly varying at long times. The frame number-dependent integration time is accounted for in the analysis. Two thousand laser shots are averaged for each frame in order to obtain good statistics. Each dataset takes approximately 2.5 min to collect. The appropriate portions of the three spatially overlapping datasets are then spliced together

to form a complete dataset covering the full range of angles.

Table 2 shows the times at which the measurements were performed, along with other measurement characteristics. The complete set of measurements was collected during an interval of approximately 50 min. The raw outcome of a WAIL measurement is a three-dimensional dataset that contains one temporal and two angular dimensions (cf. Fig. 4). We will see that the cloud field observed here had relatively high horizontal homogeneity; we, therefore, perform azimuthal averages resulting in substantial noise reduction. Only the dependencies on zenith angle and on time will be further analyzed.

5. WAIL data analysis

Figure 9 shows the time dependence of the WAIL signal detected by the central pixel with the 535-nm

TABLE 2. Timetable of measurements performed with WAIL on 25 Mar 2002. The “laser off” is the modality used to measure the background noise. The designations of 1 and 2 identify the three collections that were merged into our two analysis datasets.

Filter (nm)	Time (UTC)	Shots per time bin	Time bin width (ns)	Comment
535	0723	2000	5–100	1
	0728	2000	5–100	
	0752	2000	5–100	
	0754	2000	5–100	
	0759	2000	5–100	
540	0732	2000	50–250	1
	0809	2000	50–250	2
	0814	2000	50–250	Laser off
546	0735	5000	50–250	1
	0743	5000	50–250	Laser off
	0802	5000	50–250	2

filter at 0723, 0752, and 0759 UTC. These signals coincide well, demonstrating a high degree of horizontal homogeneity of the lower part of the cloud during the whole observation period. This statement about horizontal homogeneity is confirmed by millimeter-wavelength radar reflectivity profiles (see Fig. 14), and the

dataset shows that it can be extended to the vertical direction for our two separate three-filter collections starting, respectively, at 0728 and 0759 UTC.

At present, the theory assumes a uniform cloud, which seems to be justified for the two periods of interest identified in Table 2. This assumption guides the execution of our first task, which is to determine cloud-base height. The lidar signal that is reflected from a homogeneous slab contains a very sharp increase coinciding with the cloud’s lower boundary. Accordingly, the on-beam WAIL signal in Fig. 9 shows that cloud base is at a range of about 0.5 km.

We start with time-integrated off-beam signals—the steady-state or “cw” distribution of the reflected radiance in (10). The empirical function in (14) is used to convert the measured signal to the flux density distribution predicted by theory. Because the average cosine of the scattering angle for water-droplet clouds is ≈ 0.85 (Deirmendjian 1969; Gerber et al. 2000), we have only two uniform slab-cloud parameters to estimate: geometrical thickness H and the extinction coefficient σ , which, by multiplication, give optical thickness τ . This is done by forming a standard “observed–predicted” cost function, computed over the relevant range of $r = d_{\text{obs}}$

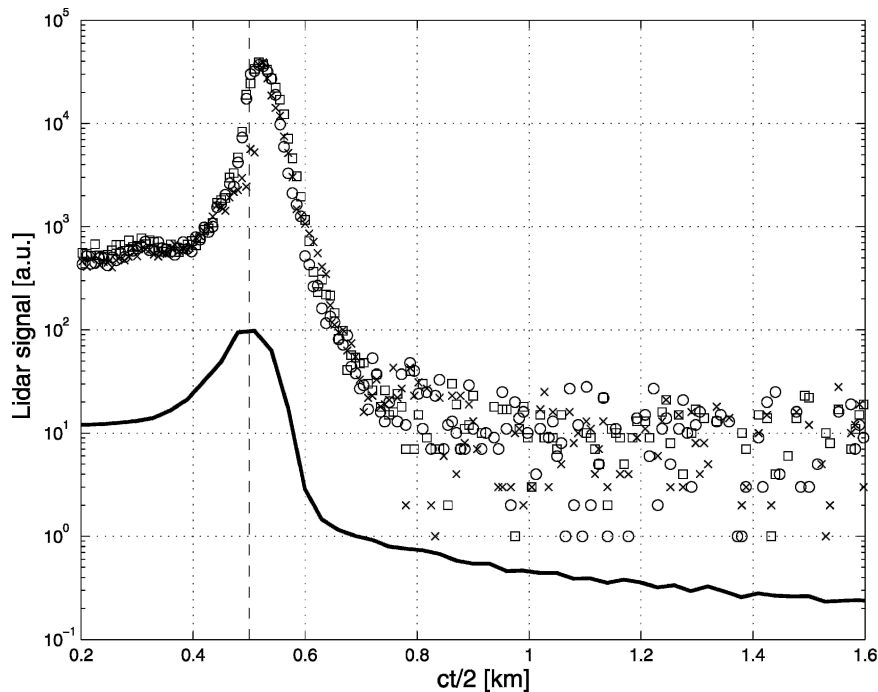


FIG. 9. The lidar signal measured by the central WAIL pixel as a function of range from the ground. Symbols correspond to different measurement times: 0723 (x), 0752 (O), and 0759 (□) UTC. The vertical dashed line marks 0.5-km range where WAIL and other instruments detect cloud base. The solid black line shows the MPL signal detected at 0800 UTC. It shows how the MPL sees a crossover from the aerosol background to cloudy air at a somewhat shorter range than the estimate from the WAIL data (based on the homogeneous slab assumption).

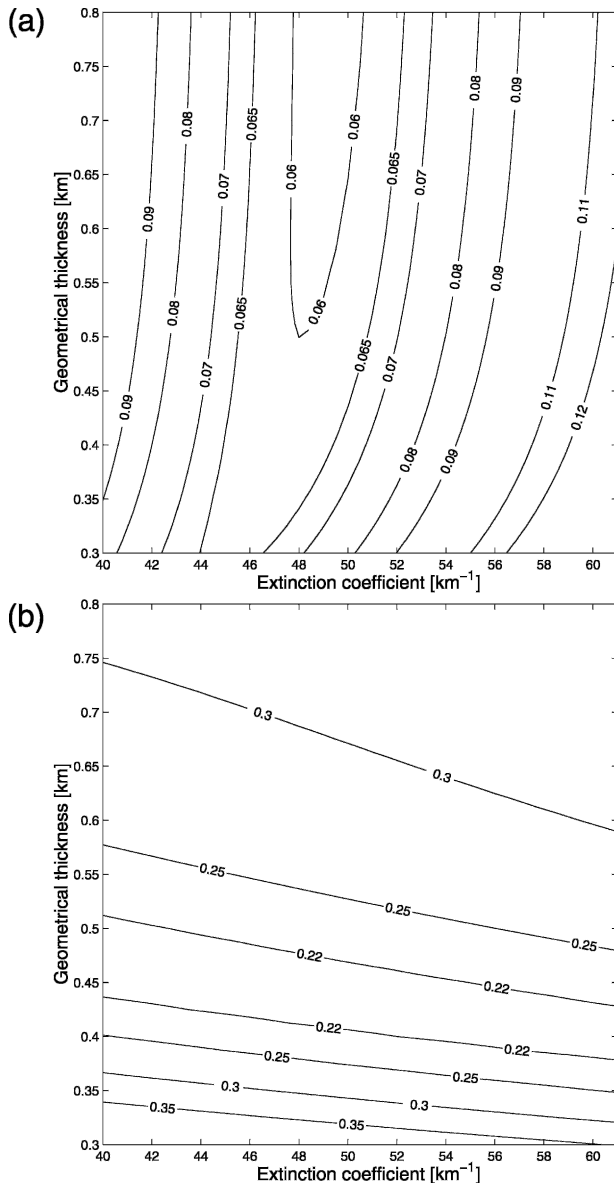


FIG. 10. Cost function for fitting the WAIL signal detected at 0730 UTC using diffusion formulas: (top) the time-integrated case and (bottom) the time-resolved case.

$\tan\theta$, which is minimized by varying the two cloud parameters. Consistent with our homogeneity assumption, we average the WAIL signal azimuthally, resulting in substantial measurement error decrease. The trivial normalization parameter in (14) is also estimated through the fitting procedure to account for the present lack of absolute calibration in WAIL. The upper panel of Fig. 10 shows the cost function for the relevant range of $\{H, \sigma\}$ using the WAIL signal measured at 0730 UTC with $10^\circ \leq \theta \leq 26^\circ$. The mostly vertical orientation of the isolines clearly shows that the time-integrated signal helps mostly to determine σ .

The same analysis is repeated for the time-resolved data and is displayed in the lower panel of Fig. 10. It shows isolines with mostly horizontal orientation and, thus, time-resolved data enable the estimation of H . In this case, we used the diffusion prediction in (6), 0730 UTC WAIL data for $\theta = 26.6^\circ$, and a range (i.e., $ct/2 + d_{\text{obs}}/\cos\theta$) between 1.0 and 1.9 km. Although our data are too truncated to estimate them, moments are consistent with these findings. Time dependence is dominated by H because τ only enters through correction terms for (1) and in higher-order moments such as (4). By the same token, variance of the horizontal transport, that is, $\langle r^2 \rangle$ from (2), goes as H/σ , so extinction changes have a first-order effect.

We can combine the advantages of both the time-resolved and time-integrated data analyses by constructing a weighted sum of the cost functions, each one being normalized naturally by its minimum. In this case, the ratio is about 4:1 in favor of the time-integrated data because of its reduced noise level. The result is in Fig. 11 (upper panel), showing a clear minimum at $H = 0.45$ km and $\sigma = 48$ km $^{-1}$. An objective analysis using nonlinear regression yields an uncertainty on σ of 3 km $^{-1}$ and 0.09 km for H . Figure 11 (lower panel) repeats this for WAIL signals detected at 0800 UTC, yielding $H = 0.6 \pm 0.2$ km and $\sigma = 50.5 \pm 3$ km $^{-1}$. The corresponding optical thickness estimates are 21.6 ± 5.7 at 0730 UTC and 30.3 ± 11.8 at 0800 UTC. The large uncertainties in the geometrical thickness and optical thickness, especially at 0800 UTC, are traceable directly to the insufficient FOV for the low cloud ceiling (combined with relatively large cloud thickness). We discuss further on a simple remedy for this situation without modifying WAIL's present specifications. To conclude the discussion of our retrieval technique, we demonstrate in Fig. 12 how the adjusted diffusion theory predictions compare with the signals measured at 0730 UTC. Note that the arrowed lines show the independent variable ranges over which the parameter fit has been performed.

6. Comparison with ARM instruments

Our WAIL measurements described and analyzed above were performed at the ARM Climate Research Facility (ACRF) in Oklahoma, where cloud observations are made routinely. ARM cloud instruments used here are the laser ceilometer, micropulse lidar, microwave radiometer, and millimeter-wavelength cloud radar. We now compare their determinations with that of WAIL.

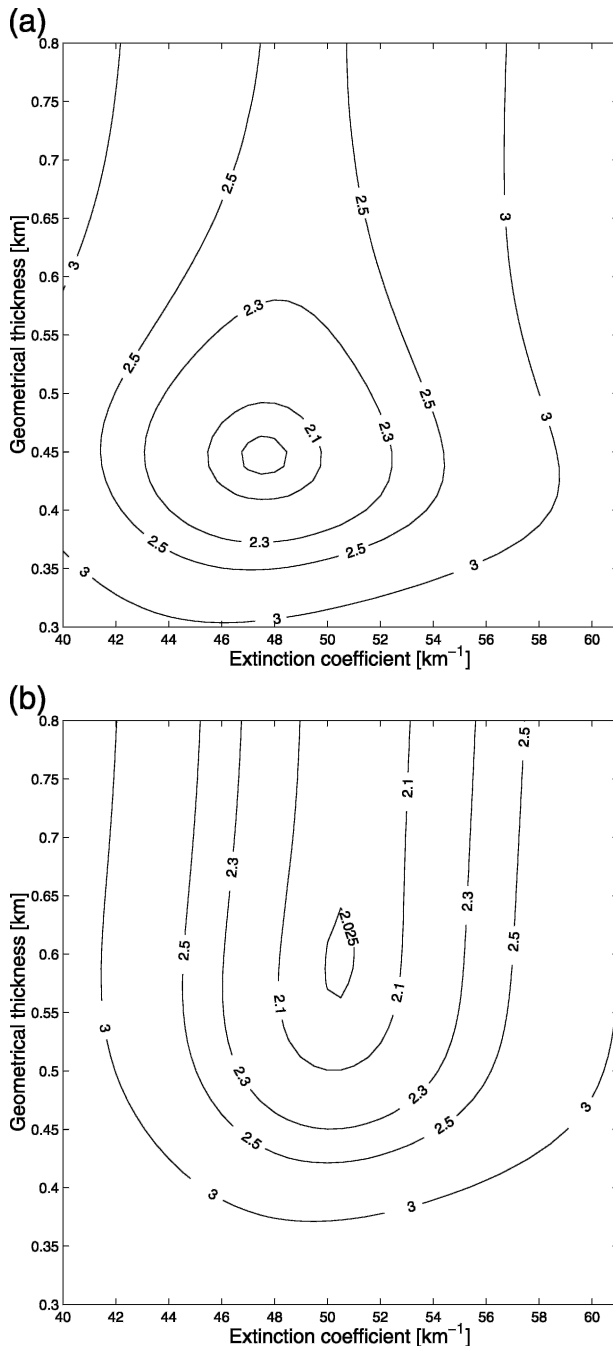


FIG. 11. Merged cost functions for fitting WAIL signals detected at (a) 0730 and (b) 0800 UTC. For the upper panel, the components are obtained from those of Fig. 10, normalized by their minima.

a. Laser ceilometer and micropulse lidar

The Vaisala Ceilometer (VCL) is a single-purpose lidar operating in near-infrared (905 nm). Ceilometer cloud-base heights of interest are depicted in Fig. 13. MPL delivers both cloud-base and cloud-top heights,

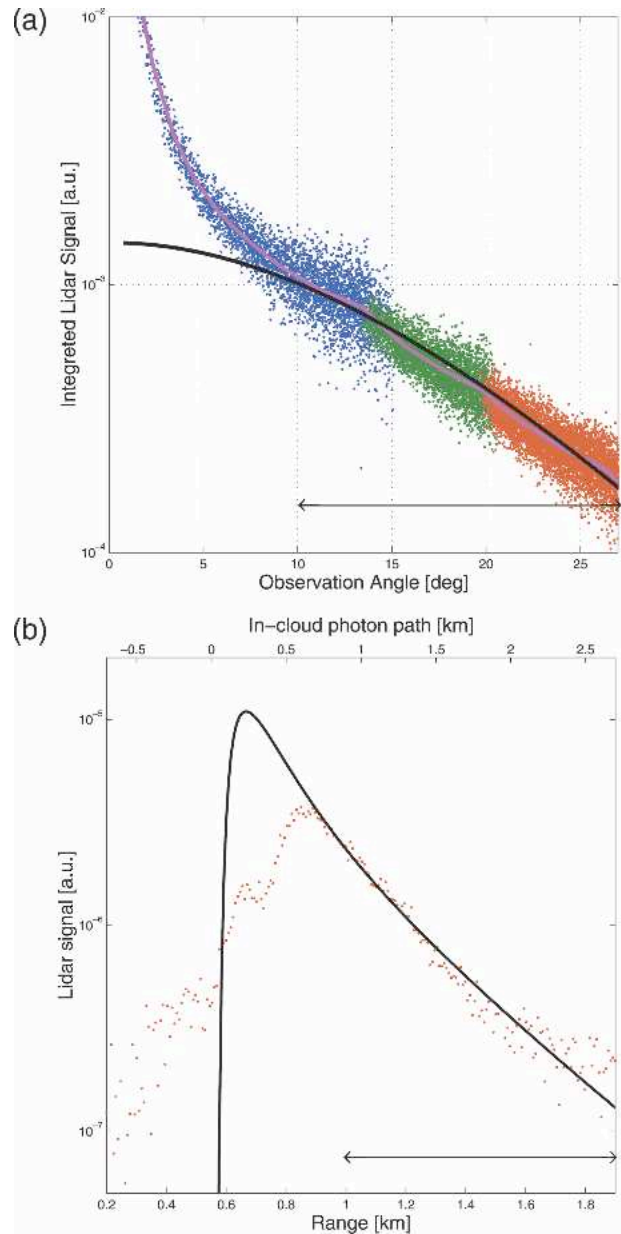


FIG. 12. (a) Time-integrated flux density as a function of the observation angle θ . The dots of three different colors correspond to WAIL radiance measurements at 0730 UTC through the three interference filters in Fig. 2 and converted to flux using the empirical factor in Eq. (14). The solid black line is the best-fit steady-state diffusion model in Eq. (10) using parameters from the corresponding panel in Fig. 11. The colored line is a running mean of the WAIL data that approximate what was used in the regression (azimuthal averages); here we plot WAIL pixel values to show their spread from natural variability as well as instrumental noise. (b) Time-resolved flux density as a function of range and in-cloud path for the narrow annulus of pixels at $\theta = 26.6^\circ$. The dashed line is the best-fit diffusion model in Eq. (6) using the same parameters as in the upper panel. The intervals highlighted along the two horizontal axes indicate the angles and times used in the nonlinear cloud parameter estimation.

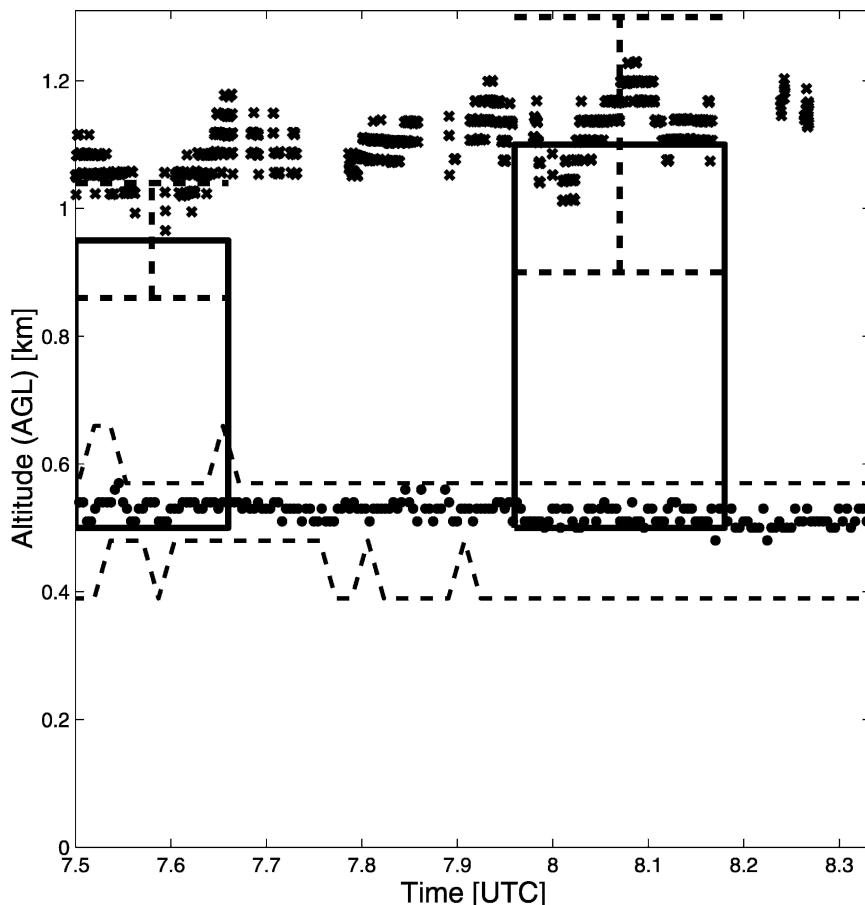


FIG. 13. Cloud-base and cloud-top heights as a function of time. The dashed lines show the heights of cloud base and top retrieved from the MPL data. The MPL cloud-top data are not reliable in the present case of an optically thick layer. The dots derive from the ceilometer. The time series for cloud top indicated by "x" symbols is from the THOR instrument (courtesy of T. Varnai and K. Yetzer); that instrument was between 1 and 40 km away from the central facility (measured horizontally) during this time period. At 0730 UTC THOR was at its closest (0.3 km horizontally) and estimated the cloud-top height to be 1.07 km. Our collection periods and retrievals of the cloud-base and -top altitude are shown by the rectangular areas while the dashed lines depict uncertainties in the cloud-top estimation.

operating at 523.5 nm (very close to WAIL's 532-nm wavelength). Cloud boundary heights from the MPL are in Fig. 13: base and top heights are dashed and dashed-dotted lines, respectively. MPL's estimation of geometrical thickness of the cloud is 0.1–0.2 km. Of course, MPL's cloud-top product is biased very low in the case of this optically thick cloud layer because it is assumed 1) that multiple scattering does not contaminate significantly the directly transmitted beam, and 2) that it can reach cloud top on a two-way trip through the cloud. Neither of these conditions is satisfied here, so we will not discuss MPL cloud tops any further.

Our two (on beam) inferences of mean cloud base in Fig. 13 are at 0.5 km; they agree with the VCL (at most, 50 m higher), but the MPL estimates are up to 100 m

lower. Although we have not examined the MPL algorithm in any detail, we attribute this systematic discrepancy between ARM instruments with the fact that extinction coefficient profiles in clouds are generally represented as increasing more-or-less rapidly from the zero level. In this case the maximum of the (on beam) lidar signal does not coincide with the cloud-base (i.e., vanishing extinction) level, and this necessarily complicates cloud-base detection. If we adopt the MPL definition of cloud base as a way of anticipating how a vertically varying model for cloud extinction would behave, then we can adjust our estimates of cloud thickness to ≈ 0.55 km at 0730 UTC and ≈ 0.7 km at 0800 UTC. This correction would not affect cloud optical thickness estimates.

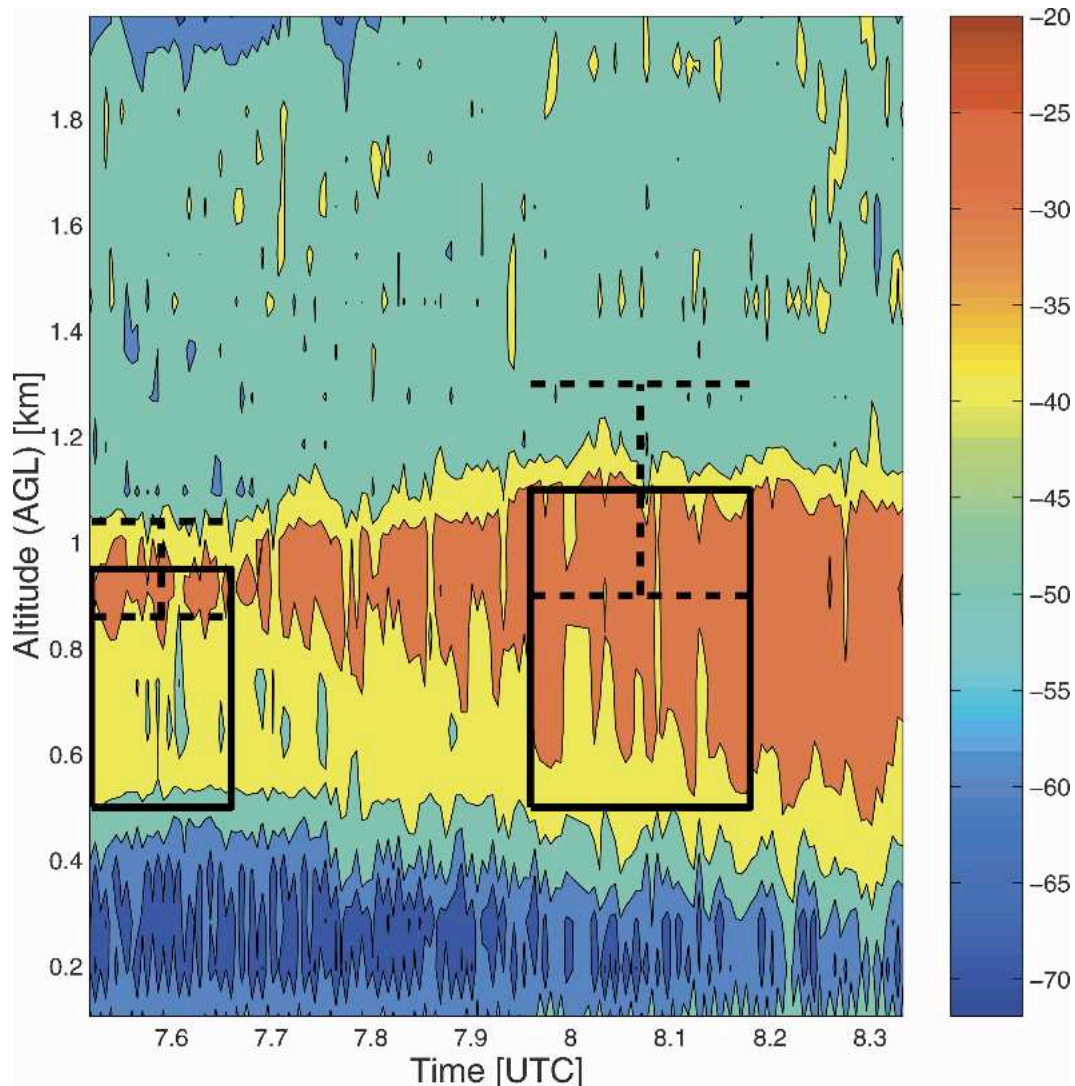


FIG. 14. Cloud reflectivity (in dBZ) as a function of time and altitude above ground level (AGL) retrieved from the MMCR data. The layer with a strong reflectivity is situated between approximately 0.4 and 1.1 km. The rectangles show the location of the cloud inferred from WAIL data (and the duration of the three-filter collection) while the dashed lines depict uncertainties in the cloud-top estimation.

b. Millimeter-wavelength cloud radar and THOR

The MMCR probes internal cloud structure and detects boundaries. The two-dimensional chart of the reflectivity in Fig. 14 characterizes the cloud's inner and outer structure during our deployment. We also plot the position of the cloud layer according to WAIL, which, accounting for our uncertainties, is close to what the MMCR sees. There is no other nearby ARM instrument providing cloud-top height. There is, however, a THOR cloud-top estimate of 1.07 km at 0718 UTC (THOR was then between 0.3 and 1.0 km away from the SGP central facility, measured horizontally), which is consistent with the MMCR reading.

For reference, Fig. 13 shows the ± 0.1 km variability of cloud-top height according to the airborne THOR lidar during our observation period. The NASA P-3 was then too far from the central facility for direct comparison with WAIL. However, we note that the cloud tops from the WAIL and THOR instruments track each other, within the variability and uncertainty.

Figures 13–14 show that our two *mean* cloud-top estimates are, if anything, 50–100 m lower than the corresponding means of the *fluctuating* MMCR and THOR counterparts. Targeting cloud thickness H , this small bias at cloud top is in addition to the one already identified at cloud base of similar magnitude. This time, however, it cannot be attributed to the vertical homo-

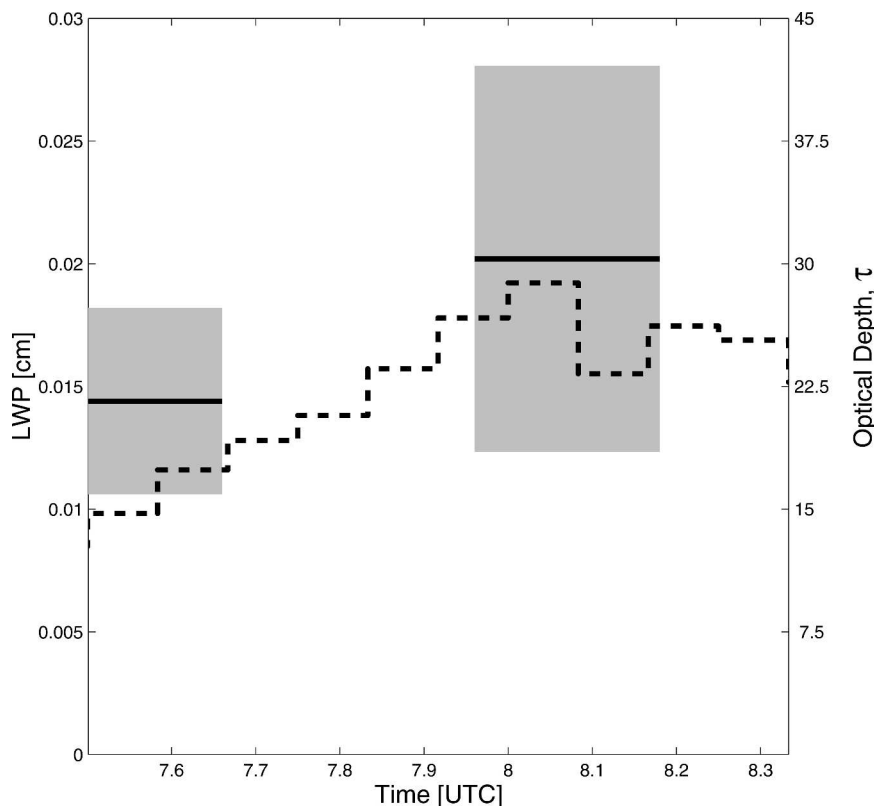


FIG. 15. (left) LWP and (right) cloud optical thickness as a function of time. The estimation of the optical thickness from the MWR data (dashed line) may have as much as 20% error due to uncertainty of the effective droplet radius (set here to $10\text{ }\mu\text{m}$ for simplicity). The horizontal solid lines show the optical thickness and associated LWP from the WAIL data while the gray patches show the estimation error.

geneity assumption (Love et al. 2001), but rather to the truncation problem. We, therefore, expect this bias to diminish along with the overall uncertainty as WAIL's FOV is widened.

c. Microwave radiometer

The MWR measures column-integrated amounts of water vapor and (cloud) liquid water. Using these data we can estimate cloud optical thickness (Stephens 1978):

$$\tau_H = \frac{3}{2} \frac{\text{LWP}}{r_e}, \quad (15)$$

where LWP is the liquid water path measured by MWR in centimeters (or millimeters), and r_e is the effective radius of the cloud particles in the same units. It is commonly assumed that $r_e \approx 10\text{ }\mu\text{m} = 10^{-3}\text{ cm}$. This estimation of optical thickness is shown in Fig. 15 vis-à-vis LWP in centimeters.

Being a vertical integral through all of the 3D variability that plagues all cloud boundary retrievals, opti-

cal depth estimation and comparison should be easier, but may not be. We estimate cloud optical thickness at ≈ 21.6 for the 0730 UTC collection and ≈ 30.3 at 0800 UTC, consistently $\approx 20\%$ over the MWR values. This suggests that r_e may have been that much less than the canonical $10\text{-}\mu\text{m}$ value used in the LWP-to- τ conversion.

d. Discussion

The above analysis of agreement and disagreement between various cloud-probing devices notwithstanding, it is important to bear in mind that the very definition of a real cloud's boundary will—and should—depend on the particulars of the instrument (wavelength, FOV, space-time sampling and averaging, etc.) as well as on the conceptual picture that the algorithm developer had in mind. Under these conditions, the tracking we get between different instruments (and even more so with the THOR instrument) is tantamount to a successful validation of the off-beam lidar technique, if not the WAIL instrument itself (more ob-

servations are needed under a wider variety of conditions).

Inasmuch as we see real disagreement between instruments, the next logical question is, of course, which instrument are we going to believe? In our view, the answer should come from the application in mind, because there rarely is some fundamental “truth” about the properties of some designated cloud. As an example, and without comprehensive analysis of all possible methods, the MWR may be the best source for LWP if the hydrological cycle is the focus. In contrast, if climate and radiation are at the scientific focus, then optical depth from WAIL may be a more judicious choice because it operates at an energetically relevant wavelength and, in sharp contrast with the MWR, no assumptions about cloud microphysics are required.

7. Summary and outlook

We analyzed WAIL data collected during a field campaign where several radically different cloud instruments were operating. Comparison of the results shows that even the simplest possible modeling assumption—that the cloud is a homogeneous slab—yields very reasonable estimates of the cloud’s geometrical characteristics: base height and geometrical thickness and hence cloud-top height. Our estimates of cloud optical thickness also coincide well with the available data. Only two values of the geometrical and optical thicknesses were obtained, one each at the beginning and end of a relatively short interval when the cloud ceiling was at its maximum of ≈ 0.5 km during the deployment. At other times, cloud base was so low that (in spite of a 57° full-width FOV) the off-beam signal was too severely truncated to even attempt cloud property retrievals. The homogeneous cloud model used here is determined only by its geometrical and optical thicknesses and can already reproduce accurately the observed space–time cloud reflectance characteristics for large enough times and distances. In this sense, the uniform model can be viewed as an optical equivalent to the real 3D cloud being probed.

Our future research will be to develop appropriate procedures to retrieve cloud structure with more fidelity by means of more complete use of WAIL’s capabilities. The logical starting point is to retrieve the extinction coefficient profile and then obtain a volume-averaged measure of the horizontal variability. We have obtained preliminary results on both accounts in the forward modeling without leaving the productive framework of diffusion theory. Additionally, presently untapped portions of WAIL signals can be exploited with small-angle multiple scattering modeling. This en-

hancement will enable more accurate determination of cloud parameters near the irradiated boundary, specifically, the extinction profile (leading to better cloud bases) and effective droplet radius.

Overall, the limited validation we obtained of the WAIL instrument based on a single case study at the ARM site is a significant milestone because there is a relatively easy way of overcoming the truncation problem that restricted the amount of useful data. This problem occurs only in ground-based configurations when the cloud base is low and is mitigated simply by using a shorter focal length lens (the current lens corresponds to a moderately wide-angle photographic lens). The angular truncation problem can be further ameliorated by tilting the receiver so that the image of the impact point of the beam on cloud base is moved from the center to a corner of the focal plane, which more than doubles the range of angles relative to the beam. This solution is possible because of the unique advantage of having an imaging device at the focal plane of the receiver. For the present fore optics, we would be going from $\theta_{\max} = 26.8^\circ$ to $\theta_{\max} \geq 55^\circ$, thus, for a cloud base at 0.5 km, we would go from a maximum off-beam distance of 0.25 to 0.87 km or better. The minor cost of this modification is a $\approx 90^\circ$ sample in azimuth (down from 360°) from a few degrees up to $\approx 60^\circ$ from zenith (using the present lens), and somewhat less at larger zenith angles. With this flexible spatial/angular sampling, we know from asymptotic diffusion theory (Polonsky and Davis 2004) that moment-based methods and single-term expansions for the response become accurate. Far simpler data analysis methods than are used here, thus, become available. Even in a thick fog scenario where cloud base is at ground level, the beam can be removed completely from the receiver’s FOV; WAIL, thus, becomes an “in situ” cloud lidar, and the time domain techniques proposed by Evans et al. (2003) apply. Another procedural simplification follows from using a single but wider-band background-suppression filter. The cost in increased background noise can easily be offset by a slightly longer exposure (now at 2.5 min).

The most exciting instrumental development by far will be the successful demonstration of filters that are narrow enough for daytime operation. We have already achieved a good signal-to-noise ratio under the full moon, which is $\approx 10^6$ times dimmer than daylight. A factor of $\approx 10^6$ improvement in background rejection is needed to maintain a comparable signal-to-noise level in full daylight. A rudimentary approach for realizing some coarsely sampled off-beam lidar results in daylight derives from the method of automatic background tracking and subtraction used for the very first detec-

tion of diffusing lidar photons (Davis et al. 1999). This early success was accomplished simply by deflecting the transmitter's beam away from the narrow (≈ 1 mrad) field of view of an otherwise quite standard zenith-pointing lidar system (≈ 0.5 J pulses at 1064 nm, 10-Hz repetition rate, 40-cm aperture). The off-beam signal was easily detected above the background noise out to 12° away from zenith in broad daylight. We are presently pursuing a solution based on an ultranarrow (≈ 0.005 nm) magneto-optic filter design that operates on one of the sodium doublet lines near 589 nm. The combination of a narrow-filter bandwidth with the existence of a strong sodium Fraunhofer absorption at precisely the same wavelength brings us close to our background rejection goal. We refer the reader to Love et al. (2002) for a recent progress report on this strategy, which calls for a tunable laser source locked at the filter-selected wavelength.

In summary, the joint WAIL and THOR campaign conducted at the ARM Southern Great Plains CART site confirmed the validity of off-beam lidar as a worthy concept in cloud remote sensing. In spite of an inconveniently low cloud base, resulting in spatially truncated photon distribution data from the ground-based WAIL, success was achieved by employing the diffusion theory of Polonsky and Davis (2004) that predicts the distribution and not just its moments. The off-beam lidar retrievals of cloud characteristics agreed well, within the established uncertainty, with independent observations of the cloud parameters. We are looking forward to seeing widespread use of off-beam (multiple scattering) lidar techniques not only for terrestrial clouds, but also for vegetation canopies (Kotchenova et al. 2003), ice, snow, and so on. Eventually, as more compact and powerful laser sources become available, observations from spacecraft will become an option. This opens up applications in planetary science, such as sounding Europa's icy surface, which is thought by some at least to be relatively thin.

Acknowledgments. We acknowledge financial support for this research by the Office of Biological and Environmental Research of the U.S. Department of Energy as part of the Atmospheric Radiation Measurement (ARM) Program and by the Laboratory-Directed Research and Development (LDRD) Program at Los Alamos. We thank Larry Tellier of LANL/ISR-2 for his invaluable help during the data collection in March 2002 where we were also supported by Jim Liljegren, John Schatz, Mike Rainwater, and Tim Grove from ARM's infrastructure team. The authors used the following ARM datasets: sgp5mwravgC1.c1.20020325.000000.cdf (MWR), sgpvceil25kC1.b1.20020325.

000005.cdf (ceilometer), sgpmp1nor1campC1.c1.20020325.000010.cdf (MPL), and sgpmmrcalC1.a1.20020325.000000.cdf (MMCR).

We also thank Tamas Varnai and Ken Yetzer from whom we received cloud-top estimates by the airborne THOR lidar. Interactions with the THOR instrument team (Robert Cahalan, John Kolasinski, Ken Yetzer) during the validation campaign were particularly exciting. Finally, we thank Luc Bissonnette, Bob Cahalan, Ed Eloranta, Frank Evans, Lee Harrison, Cheng Ho, Sasha Marshak, Matt McGill, Chuck Rohde, Jim Spinhirne, Dave Winker, and Warren Wiscombe for many stimulating discussions about off-beam lidar concepts.

REFERENCES

- Bissonnette, L. R., 1996: Multiple-scattering lidar equation. *Appl. Opt.*, **35**, 6449–6465.
- , G. Roy, L. Poutier, S. G. Cober, and G. A. Isaac, 2002: Multiple-scattering lidar retrieval method: Tests on Monte Carlo simulations and comparisons with in situ measurements. *Appl. Opt.*, **41**, 6307–6324.
- Cahalan, R. F., and J. B. Snider, 1989: Marine stratocumulus structure during FIRE. *Remote Sens. Environ.*, **28**, 95–107.
- , M. J. McGill, J. Kolasinski, T. Varnai, and K. Yetzer, 2005: THOR—Cloud thickness from off-beam lidar returns. *J. Atmos. Oceanic Technol.*, **22**, 605–627.
- Clothiaux, E. E., M. A. Miller, B. A. Albrecht, T. P. Ackerman, J. Verlinde, D. M. Babb, R. M. Peters, and W. J. Syrett, 1995: An evaluation of a 94-GHz radar for remote sensing of cloud properties. *J. Atmos. Oceanic Technol.*, **12**, 201–229.
- Davis, A. B., 1999: Physical thickness and optical depth of stratocumulus from space-borne lidar, A moment-based diffusion method. *OSA Topical Meeting "Optical Remote Sensing of the Atmosphere,"* Santa Barbara, CA, Optical Society of America, 66–68.
- , and A. Marshak, 2002: Space-time characteristics of light transmitted by dense clouds: A Green's function analysis. *J. Atmos. Sci.*, **59**, 2713–2727.
- , —, R. Cahalan, and W. Wiscombe, 1997a: The Landsat scale break in stratocumulus as a three-dimensional radiative transfer effect: Implications for cloud remote sensing. *J. Atmos. Sci.*, **54**, 241–260.
- , D. M. Winker, A. Marshak, J. D. Spinhirne, R. F. Cahalan, S. Love, S. H. Melfi, and W. J. Wiscombe, 1997b: Retrieval of physical and optical cloud thicknesses from space-borne and wide-angle lidar. *Advances in Atmospheric Remote Sensing with Lidar*, A. Ansmann et al., Eds., Springer-Verlag, 193–196.
- , C. Ho, and S. P. Love, 1998: Off-beam (multiply-scattered) lidar returns from stratus, 2: Space-time measurements in a laboratory simulation. *Proc. 19th Int. Laser Radar Conf.*, Annapolis, MD, NASA Center for Aero-Space Information, 55–58.
- , R. F. Cahalan, J. D. Spinhirne, M. J. McGill, and S. P. Love, 1999: Off-beam lidar: An emerging technique in cloud remote sensing based on radiative Green-function theory in the diffusion domain. *Phys. Chem. Earth B*, **24**, 177–185; Erratum 757–765.
- , D. M. Winker, and M. A. Vaughan, 2001: First retrievals of dense cloud properties from off-beam/multiple-scattering li-

- dar data collected in space. *Laser Remote Sensing of the Atmosphere: Selected Papers from the 20th International Conference on Laser Radar*, A. Dabas and J. Pelon, Eds., Ecole Polytechnique, 35–38.
- Deirmendjian, D., 1969: *Electromagnetic Scattering on Spherical Polydispersions*. American Elsevier, 290 pp.
- Eddington, A. S., 1916: On the radiative equilibrium of stars. *Mon. Not. Roy. Astron. Soc.*, **77**, 16–35.
- Einstein, A., 1905: On the motion, required by the molecular-kinetic theory of heat, of particles suspended in a fluid at rest. *Ann. Phys.*, **17**, 549–560.
- Evans, K. F., R. P. Lawson, P. Zmarzly, D. O'Connor, and W. J. Wiscombe, 2003: In situ cloud sensing with multiple scattering lidar: Simulations and demonstration. *J. Atmos. Oceanic Technol.*, **20**, 1505–1522.
- Gerber, H., Y. Takano, T. J. Garrett, and P. V. Hobbs, 2000: Nephelometer measurements of the asymmetry parameter, volume extinction coefficient, and backscatter ratio in Arctic clouds. *J. Atmos. Sci.*, **57**, 3021–3034.
- Ishimaru, A., 1978: *Wave Propagation and Scattering in Random Media*. Academic Press, 572 pp.
- King, M. D., 1986: Multiwavelength scanning radiometer from airborne measurements of scattered radiation within clouds. *J. Atmos. Oceanic Technol.*, **3**, 513–522.
- , L. F. Radke, and P. V. Hobbs, 1990: Determination of the spectral absorption of solar radiation by marine stratocumulus clouds from airborne measurements within clouds. *J. Atmos. Sci.*, **47**, 894–907.
- Kotchenova, S. Y., N. V. Shabanov, Y. Knyazikhin, A. B. Davis, R. Dubayah, and R. B. Myneni, 2003: Modeling lidar waveforms with time-dependent stochastic radiative transfer theory for remote estimations of forest biomass. *J. Geophys. Res.*, **108**, 4484–4496.
- Liljegren, J. C., 1994: Two-channel microwave radiometer for observations of total column precipitable water vapor and cloud liquid water path. Preprints, *Fifth Symp. on Global Change Studies*, Nashville, TN, Amer. Meteor. Soc., 262–269.
- Lonnqvist, J., 1995: Experiences with a novel single-lens cloud height lidar. Preprints, *Ninth Symp. on Meteorological Observations and Instrumentation*, Charlotte, NC, Amer. Meteor. Soc., 106–109.
- Love, S. P., A. B. Davis, C. A. Rohde, and C. Ho, 2001: Remote sensing of cloud thickness and liquid water content with wide-angle imaging lidar. *Atmos. Res.*, **59**, 295–312.
- , —, —, L. Teller, and C. Ho, 2002: Active probing of cloud multiple scattering, optical depth, vertical thickness, and liquid water content using wide-angle imaging lidar. *Proc. SPIE*, **4815**, 129–138.
- Marshak, A., A. Davis, W. J. Wiscombe, and R. F. Cahalan, 1995: Radiative smoothing in fractal clouds. *J. Geophys. Res.*, **100**, 26, 247–26, 261.
- Meador, W. E., and W. R. Weaver, 1980: Two-stream approximations to radiative transfer in planetary atmospheres: A unified description of existing methods and a new improvement. *J. Atmos. Sci.*, **37**, 630–643.
- Miller, S. D., and G. L. Stephens, 1999: Multiple scattering effects in the lidar pulse stretching problem. *J. Geophys. Res.*, **104**, 22 205–22 219.
- Min, Q. L., and L. C. Harrison, 1996: Cloud properties derived from surface MFRSR measurements and comparison with GOES results at the ARM SGP site. *Geophys. Res. Lett.*, **23**, 1641–1644.
- Moran, K. P., B. E. Martner, M. J. Post, R. A. Kropfli, and D. C. Welsh, 1998: An unattended cloud-profiling radar for use in climate research. *Bull. Amer. Meteor. Soc.*, **79**, 443–455.
- Nakajima, T. Y., and M. D. King, 1990: Determination of the optical thickness and effective particle radius of clouds from reflected solar radiation measurements. Part I: Theory. *J. Atmos. Sci.*, **47**, 1878–1893.
- Polonsky, I. N., and A. B. Davis, 2004: Lateral photon transport in dense scattering and weakly-absorbing media of finite thickness: Asymptotic analysis of the Green functions. *J. Opt. Soc. Amer. A*, **21**, 1018–1025.
- , and —, 2005: Off-beam cloud lidar: A new diffusion model and an analysis of LITE returns. Los Alamos National Laboratory Unclassified Report LA-UR-05-0794, 13 pp.
- Priedhorsky, W. C., R. C. Smith, and C. Ho, 1996: Laser ranging and mapping with a photon-counting detector. *Appl. Opt.*, **35**, 441–452.
- Schuster, A., 1905: Radiation through a foggy atmosphere. *Astrophys. J.*, **21**, 1–22.
- Spinhirne, J. D., 1993: Micro-pulse lidar. *IEEE Trans. Geosci. Remote Sens.*, **31**, 38–55.
- Stephens, G. L., 1978: Radiation profiles in extended water clouds. II: Parameterization schemes. *J. Atmos. Sci.*, **35**, 2123–2132.
- Zege, E. P., I. L. Katsev, and I. N. Polonsky, 1994: Analytical solution to LIDAR return signals from clouds with regard to multiple scattering. *Appl. Phys.*, **B58**, 345–353.